

Biexciton fine structure in monolayer transition metal dichalcogenides

M lexander Steinhoff ^{1*}, Matthias Florian¹, Mkshay Singh ¹^{2,5}, Kha Tran², Mirco Kolarczik³, Sophia Helmrich³, Mlexander W.Mchtstein³, Ulrike Woggon³, Nina Owschimikow³, Frank Jahnke¹⁴ and Xiaoqin Li²

The optical properties of atomically thin transition metal dichalcogenide (TMDC) semiconductors are shaped by the emergence of correlated many-body complexes due to strong Coulomb interaction. Exceptional electron-hole exchange predestines TMDCs to be used to study fundamental and applied properties of Coulomb complexes such as valley depolarization of excitons and fine-structure splitting of trions. Biexcitons in these materials are less well understood and it has been established only recently that they are spectrally located between excitons and trions. Here we show that biexcitons in monolayer TMDCs exhibit a distinct and rich fine structure on the order of millielectronvolts due to electron-hole exchange. Ultrafast pump-probe experiments on monolayer WSe₂ reveal decisive biexciton signatures and a fine structure in excellent agreement with a microscopic theory. We provide a pathway to understand the complex spectral structure of higher-order Coulomb complexes in TMDCs going beyond the usual classification scheme in terms of four-particle configurations.

he exchange interaction between electrons and holes in semiconductors has long been of interest in both theory and experiment. It has been discussed in the context of longitudinal-transverse exciton splitting in bulk materials^{1,2} and of exciton fine-structure splitting in quantum dots, where it is a major limitation to the generation of entangled photons^{3,4}. Biexcitons, also known as exciton molecules, are fundamental to the nonlinear optical response of semiconductors. Based on a many-body theory including biexcitonic effects, nonlinear pump-probe experiments in InGaAs quantum wells have been successfully described^{5,6} without taking electron-hole exchange into account. On the other hand, several authors have recognized the relevance of electronhole exchange for biexcitons in materials such as CuCl and CdS⁷⁻¹³. Although, in some cases, significant corrections of biexciton binding energy due to electron-hole exchange have been reported, a fine-structure splitting of biexcitons has not been discussed. Atomically thin TMDC semiconductors offer new possibilities for studying Coulomb correlation effects by introducing reciprocalspace valleys as a new degree of freedom selectively addressable by circularly polarized light. Electron-hole exchange has strong implications for the valley dynamics and is currently an object of intense research14-18. The theory of electron-hole exchange in TMDC semiconductors has been put on a microscopic basis by Qiu et al. 19, who discussed the resulting non-analytic exciton dispersion and large splitting between bright and dark excitons. In stark contrast to, for example, InGaAs quantum wells, the splitting between exciton states can reach several tens of millielectronvolts in TMDCs. Similarly strong effects are observed in the fine-structure splitting of interand intra-valley trions in these materials²⁰⁻²². It is worth speculating whether biexcitons and even higher complexes could also have a fine structure with implications for nonlinear optical effects utilized in coherent control schemes23 and for manipulation of exciton spin

coherences²⁴. However, even modern variational approaches that have been applied to describe biexcitons in TMDC semiconductors rely on simple band structures and Coulomb interaction models, neglecting electron-hole exchange effects entirely²⁵⁻²⁸.

Here, we provide evidence for a pronounced biexciton fine structure in TMDC semiconductors by performing material-realistic calculations of biexciton spectra including electron-hole exchange interaction. We condense the full microscopic theory into a simple four-particle-configuration model for biexcitons to identify the relevant interaction processes and optical selection rules. Our theory shows that the biexciton fine structure leading to several optically bright transitions is caused by nonlocal electron-hole exchange acting at a distance of multiple unit cells. On the other hand, local exchange between carriers within the same unit cell leads to an increase of the binding energy of the lowest biexciton state. Ultrafast pump-probe experiments performed on monolayer WSe, verify the theoretical prediction by showing a distinct biexciton fine structure in excellent quantitative agreement with the calculated spectrum. All biexciton resonances are found to be spectrally located between excitons and trions, which is consistent with the spectral ordering observed in monolayer MoSe, by two-dimensional coherent spectroscopy²⁹. Previously, larger biexciton binding energies have been inferred from experimental observations of other stable many-body. states in TMDCs30-36. As discussed in ref. 37, resonances in monolayer WSe2 and WS2 with binding energies larger than 50 meV can be explained by the coupling of excitons to inter-valley plasmons. Our results not only provide a more accurate description of biexcitons but also give rise to a new picture of multi-exciton states as quantum superpositions of many-body configurations going beyond the usual classification in terms of band-structure valleys. Our study may stimulate future experiments to observe fine structures also in higher-order Coulomb complexes.

¹Institut für Theoretische Physik, Universität Bremen, Bremen, Germany. ²University of Texas at Mustin, Mustin, TX, USM. ³Institut für Optik und Mtomare Physik, Technische Universität Berlin, Berlin, Germany. ⁴MMPEX Center for Materials and Processes, Universität Bremen, Bremen, Germany. ⁵Present address: Department of Material Science and Engineering, Massachusetts Institute of Technology, Cambridge, MM, USM.

^{*}e-mail: asteinhoff@itp.uni-bremen.de

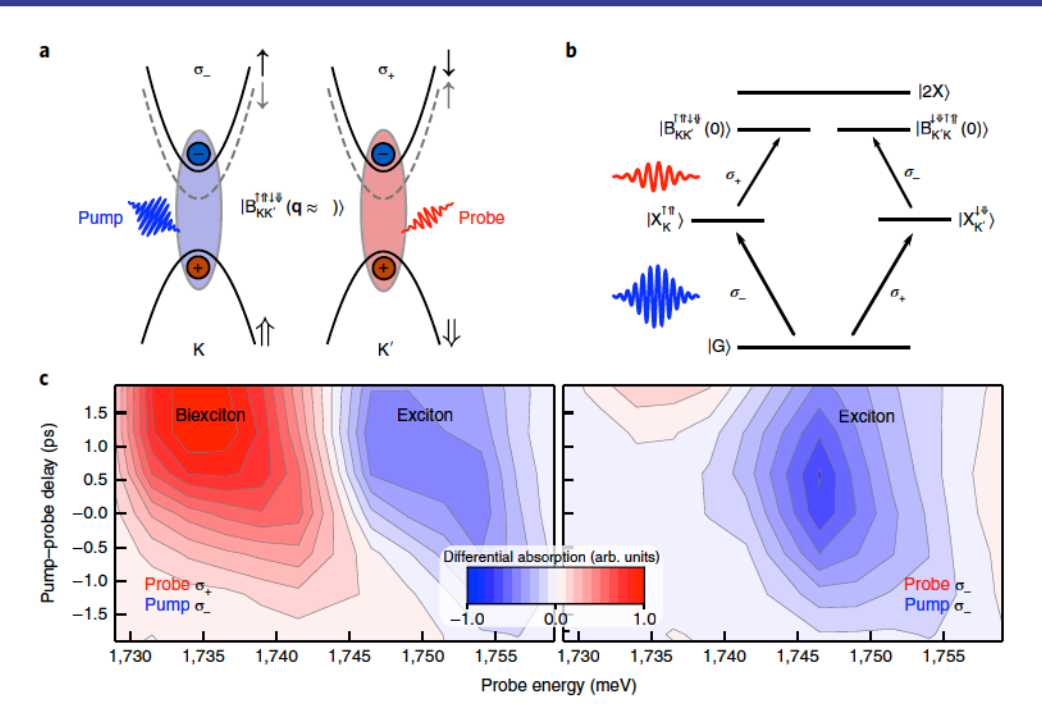


Fig. 1 | Pump-probe selection rules of biexcitons in monolayer TMDC. a, Coherent biexcitons with zero total momentum are resonantly excited by pump and probe photons with cross-circular polarization. The solid parabolas denote the relevant like-spin conduction and valence bands around the K and K' points, while the dashed parabolas denote split-off conduction bands with unlike spins. The biexciton state $|B_{KK}^{\uparrow \uparrow \uparrow \downarrow \downarrow}(q \approx 0)\rangle$ emerges from the mutual Coulomb interaction of two electrons and two holes and can be pictured as being composed of two excitons in the K and K' valleys with small momenta around q = 0. The arrows denote the electron (†) and hole (†) spins of the contributing excitons. b, M schematic of a pump-probe experiment with two equivalent excitation pathways leading to two equivalent bright biexciton states. The biexciton binding energy is given by the difference between the biexciton energy and the exciton-exciton scattering continuum edge denoted by $|2X\rangle$. c, Differential absorption of WSe₂ pumped at the red wing of its neutral exciton resonance in a pump-probe experiment with cross- (left panel) and co-circularly polarized (right panel) pump and probe pulses.

Biexcitons can be detected in nonlinear optical measurements, where biexciton formation can either take place coherently or incoherently. In the latter case, the semiconductor is excited above the single-particle bandgap to generate hot carriers that may relax and form excitons and biexcitons by passing excess energy to the lattice before carrier recombination sets in. In a resonant pump-probe experiment, a pump tuned to the exciton energy leads to an induced absorption of the probe, tuned to the energy redshifted from the pump by the biexciton binding energy6. This coherent process of biexciton creation is cleaner and easier to compare with a microscopic theory. The measured pump-probe signal is governed by optical selection rules that typically allow the observation of biexcitons only for certain combinations of pump and probe polarizations. In atomically thin TMDC semiconductors, K and K' valleys are linked by time-reversal symmetry. Furthermore, strong spinorbit splitting of the valence band leads to spin-valley locking, and thus valleys can be selectively excited with circularly polarized light³⁸. As is known from conventional semiconductors, biexcitons can be excited only when pump and probe photons have opposite polarization34, as illustrated in Fig. 1. For a co-circular pump-probe, no biexciton signal is expected. To test this prediction, we perform near-resonant pump-probe experiments on a mechanically exfoliated WSe₂ monolayer kept at a temperature of 13 K. For details of the experiment, see the Methods. The results of measurements with cross- and co-circular polarization of pump and probe pulses are shown in the left and right panels of Fig. 1c, respectively. As will be shown later, biexcitons in this material appear in the spectral region between the neutral exciton and the trion. Indeed, the experiment shows a distinct induced absorption in this spectral region, which is present only for cross-circular polarized pump and probe pulses. A set of pump-probe experiments over an extended spectral and time range are shown in the Supplementary Information.

For a qualitative description of the observed absorption feature, we introduce a simple yet powerful model based on a small Hilbert space of four-particle configurations to analyse the effect of electron-hole exchange on biexciton spectra. The model is underpinned by a microscopic theory of biexcitons, which we discuss in detail in the Methods and use to obtain precise numbers that can be compared to experiment. In pump-probe experiments, only biexcitons with vanishing total momentum can be observed. Due to translational symmetry of the crystal, biexcitons with different total momentum do not couple to each other, so that we can limit the Hilbert space of our model to biexcitons with vanishing total momentum. Moreover, monolayer WSe, exhibits a conductionband splitting of tens of millielectronvolts at the K-point due to spinorbit interaction as schematically shown in Fig. 1a. Due to the large conduction-band splitting, coupling between the upper and lower. conduction band is expected to be weak. Hence, we can exclude the lower conduction band from our theory, which significantly simplifies the discussion of the results. Consequently, in the subspace of zero-momentum biexcitons there are six degenerate configurations including biexcitons composed of two inter-valley excitons with opposite momentum $|K-\vec{K}|$ presented in Fig. 2a: $\{|B_{KK}^{\uparrow\uparrow\uparrow\uparrow\uparrow}(0)\rangle, |B_{KK}^{\uparrow\downarrow\downarrow\downarrow}(0)\rangle, |B_{KK}^{\downarrow\downarrow\downarrow\uparrow\uparrow}(0)\rangle, |B_{KK}^{\downarrow\downarrow\downarrow\downarrow\uparrow}(0)\rangle, |B_{KK}^{\downarrow\downarrow\downarrow\downarrow}(0)\rangle\}$. Note that microscopically biexcitons can be interpreted as superpositions of two-exciton states with different exciton momenta, just as excitons are composed of electrons and holes in different Bloch states. The exciton momentum assigned to the biexciton configurations in brackets denotes the dominant contribution to the superposition. Only the configurations $|B_{KK}^{\uparrow\uparrow\downarrow\downarrow}(0)\rangle$ and $|B_{KK}^{\downarrow\downarrow\uparrow\uparrow\uparrow}(0)\rangle$ corresponding to the pump-probe excitation pathways shown in Fig. 1b have non-zero oscillator strength. Nevertheless, all six configurations are eigenstates with energy E of the four-particle Hamiltonian H_0 NM TURE PHYSICS MRTICLES

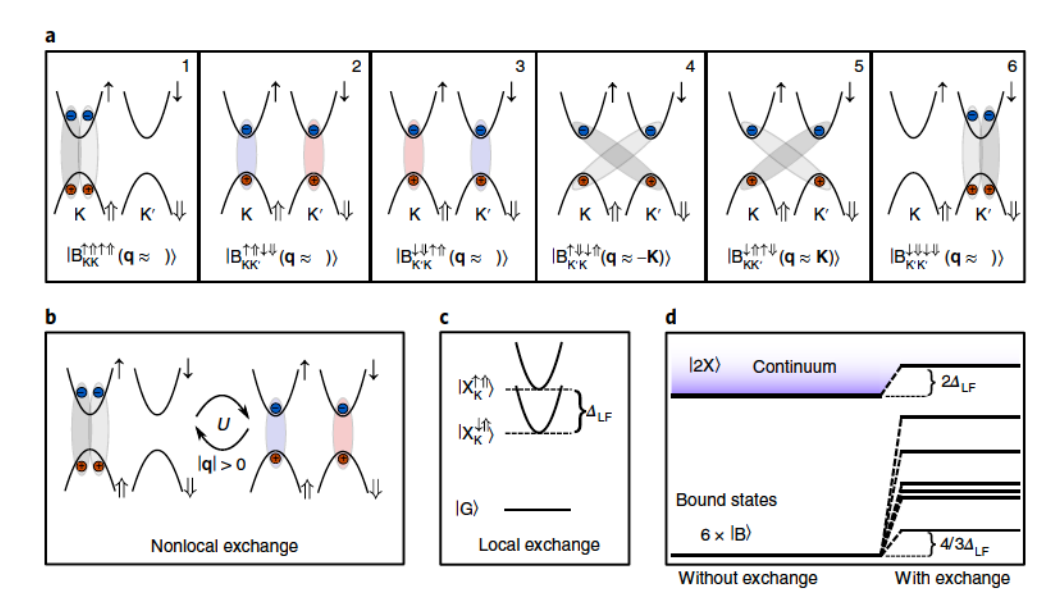


Fig. 2 | Configuration picture of biexcitons in monolayer WSe₂. **a**, Biexciton configurations realized by pairing like- and unlike-spin excitons in monolayer TMDC. Biexcitons are composed of excitons with different total momenta, just as excitons are composed of carriers in different Bloch states, where **q** denotes the dominant momentum contribution. Only two of the configurations (2 and 3) can be optically excited in a pump-probe experiment as shown in Fig. 1. **b**, Nonlocal electron-hole exchange induces interaction, given by the matrix element U, between biexciton configurations that differ by the spin flip of one electron-hole pair. M s explained in the text, U incorporates exchange processes between K and K' excitons with all finite total momenta according to their admixture in the respective biexciton states. The momentum-dependence of electron-hole exchange is discussed in the Supplementary Information. **c**, Local electron-hole exchange induces a blueshift Δ_{LF} of like-spin (triplet) excitons leading to a singlet-triplet exciton splitting. The blueshift is transferred to biexciton configurations composed of two like-spin excitons (configurations 1, 2, 3 and 6). **d**, M schematic four-particle energy spectrum including six degenerate biexciton configurations as introduced in **a** below the exciton-exciton scattering continuum. Local electron-hole exchange interaction shifts the continuum by $2\Delta_{LF}$, while nonlocal exchange leads to a fine structure of biexciton states by mixing all configurations. The shift of the lowest biexciton state by $4/3\Delta_{LF}$ can be qualitatively understood from the configuration-interaction model, while precise numbers are obtained from a microscopic theory, see discussion in the text.

that contains the kinetic energies of two electrons and two holes as well as the direct Coulomb interaction between them in analogy to the hydrogen molecule. By adding electron-hole exchange to this picture, we introduce interaction between the configurations leading to new eigenstates and eigenenergies. This concept of interacting configurations is well known from many-electron atoms or semiconductor quantum dots. It is the new eigenstates including interaction that are observed in experiment instead of the configurations. All six configurations are coupled by electronhole exchange and are thus necessary to be included in the model. Microscopically, there are local and nonlocal contributions to electron-hole exchange. Nonlocal exchange mixes excitons in the K and K' valleys with finite total momentum, thereby reducing valley selectivity¹⁴⁻¹⁷. At the same time, a non-analytic light-like exciton dispersion for like-spin excitons emerges together with a momentum-dependent splitting. Local exchange, on the other hand, leads to an overall blueshift of like-spin excitons, which we refer to as a local-field effect. A detailed discussion of electron-hole exchange in monolayer MoS2 is given in ref. 19 and comparable numerical results for monolayer WSe2 are shown in Supplementary Fig. 2. The effects of electron-hole exchange on biexciton configurations are schematically explained in Fig. 2b,c. The nonlocal and local contributions to exchange are described by the Hamiltonians H_U and H_{LP} respectively, which have to be added to H_0 . We set up the total Hamiltonian by using the six configurations as a basis:

$$H_{ij} = \langle B_i | H_0 | B_j \rangle + \langle B_i | H_U + H_{LF} | B_j \rangle$$

= $E + U_{ij} + \Delta_{LF,ij}$ (1)

The off-diagonal matrix elements take into account the spin-selection rules due to electron and hole spins in the configurations. To obtain an analytically solvable problem, we assume that all non-zero exchange matrix elements have the same values U and Δ_{LF} respectively. The full Hamiltonian is given in the Methods. It is important to realize that the matrix elements U_{ij} and $\Delta_{\mathrm{LF}ij}$ are projections of the microscopic four-particle Hamiltonian into the configuration basis and therefore incorporate electron–hole exchange between carriers with all possible momenta according to their admixture in the respective biexciton state. While nonlocal electron–hole exchange has no effect on excitons with zero total momentum, it strongly modifies the exciton dispersion at finite momenta¹⁹. We first analyse the biexciton spectrum in the absence of local-field effects by diagonalizing H_0+H_{U} , obtaining the eigenvalues

$$\{E_1 = E, E_2 = E + 2U, E_3 = E + 2U,\}\$$

 $\{E_4 = E + 2U, E_5 = E + 4U, E_6 = E + 6U\}$ (2)

Hence, without local-field effects, the lowest biexciton energy, E, remains unchanged by exchange interaction. At the same time, a triplet of states is split by twice the exchange matrix element U. Including local-field effects perturbatively via $H_{\rm LIP}$ we find the first-order energy correction to the lowest eigenenergy to be $4/3\Delta_{\rm LIP}$. The lowest eigenstate is thus shifted less than the exciton–exciton scattering continuum ($2\Delta_{\rm LIP}$) as illustrated in Fig. 2d. This is due to the fact that the unlike-spin biexciton configurations 4 and 5 in Fig. 2a are mixed into the new eigenstates but do not experience any local-field shift. The net result is an increase of the largest

binding energy by $2/3\Delta_{\rm LP}$ in good agreement with our full microscopic solution.

We draw conclusions about the oscillator strength of the interacting states under cross-circular excitation by calculating dipole matrix elements:

$$\begin{aligned} |\mathbf{d}_{i}|^{2} &= |\langle \phi_{i} | \sigma_{+} | \mathbf{X}_{K}^{\uparrow \uparrow} \rangle|^{2} \\ &= |\langle \phi_{i} | \mathbf{B}_{KK}^{\uparrow \uparrow \downarrow \downarrow \downarrow} (\mathbf{0}) \rangle + \langle \phi_{i} | \mathbf{B}_{KK}^{\downarrow \downarrow \uparrow \uparrow \uparrow} (\mathbf{0}) \rangle|^{2} \end{aligned}$$
(3)

where $|\phi_i\rangle$ are the eigenstates including nonlocal electron-hole exchange and σ_+ creates an electron-hole pair at K' as shown in Fig. 1b. It follows that three of the biexciton states including exchange interaction are bright with $|\mathbf{d}_1|^2 = 2/3$, $|\mathbf{d}_2|^2 = 1$ and $|\mathbf{d}_6|^2 = 1/3$ corresponding to the eigenenergies E_1 , E_2 and E_6 given above. This remains true in the presence of local-field effects, although the values of dipole matrix elements change. We therefore expect to observe three bound biexcitons, which are quantum superpositions of the basic four-particle configurations, with different oscillator strengths. We emphasize that the oscillator strengths (1, 2/3, 1/3) are calculated from the configuration model with the approximation that the exchange matrix elements U do not depend on the configuration indices. Furthermore, we neglected local-field effects to simplify the discussion. Hence, these oscillator strengths are expected to just give a qualitative clue about transitions being bright or dark, similar to the role that is played by the simple biexciton spectrum given in equation (2). A quantitative agreement with the actual oscillator strengths in experiment is not expected.

The above prediction of a biexciton fine structure is confirmed by additional experimental data. In Fig. 3a we present time-resolved differential absorption data obtained from the cross-polarized pump-probe signal exhibiting distinct signatures of excitons and trions as well as an additional resonance between them as a function of delay versus probe energy with a fixed pump energy of 1,744 meV. In Fig. 3b, a series of spectra with variable pump energy (from 1,759 meV to 1,741 meV) at zero delay are shown as a function of probe energy. Biexciton signatures are expected to show up as positive signals, as they result from induced absorption. The experimental data can be perfectly described by fitting curves that take into account three biexciton resonances with binding energies 18.3 ± 0.5 meV, 10.3 ± 0.5 meV and 3 ± 0.5 meV, respectively. For the fitting, while the amplitudes of each biexciton resonance are allowed to vary with changing pump-pulse energies, the centre biexciton consistently has the strongest amplitude as estimated from our configuration model. For further details of the fitting process, see the Supplementary Information. In addition to the biexcitons, our fit takes into account the differential exciton absorption resonance. We allow for a pump-induced energy shift, absorption bleaching and asymmetry of the line shape, where the line becomes narrower on the red side and wider on the blue side. The line shape asymmetry is required to understand the signatures between 1,750 and 1,755 meV that can be fitted systematically for all pump wavelengths, which we illustrate for an example in Fig. 3b,c. The exciton line asymmetry can be attributed to dephasing processes due to biexciton scattering states as discussed in refs 6,39.

After comparing the predictions of our configuration model with differential absorption spectra on a qualitative level, we further substantiate our results by a quantitative assessment of biexciton binding energies. A full microscopic description of coherent biexcitons is obtained from a generalized four-particle Schrödinger equation in reciprocal space including realistic band structures and Coulomb matrix elements. Electron–hole exchange interaction can be systematically taken into account, which is beyond modern variational approaches previously applied to TMDC semiconductors^{25–28}. By diagonalizing the full microscopic Hamiltonian, we obtain energies

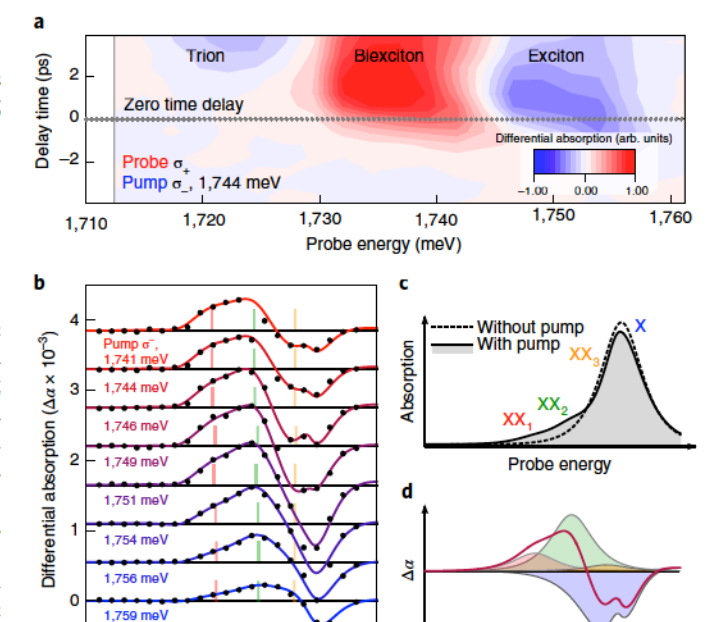


Fig. 3 | Differential absorption of monolayer WSe₂ on sapphire from theory and experiment. a, Time-resolved differential absorption data from cross-polarized pump-probe spectroscopy with a pump energy of 1,744 meV. b, The corresponding differential absorption spectra at zero time delay (filled black circles) for pump-pulse energies ranging from 1,759 meV (bottom) to 1,741 meV (top) are compared to fits based on the predictions of our theoretical model (solid lines). Details on the fits are given in the text. The different data sets are vertically shifted for better visibility, with the zero differential absorption for each pump spectrum indicated as thin lines. The vertical bars denote the spectral positions of the three optically bright biexciton states. c, Fit function for absorption spectra without and with the pump at 1,746 meV. The pump-induced emergence of asymmetry of the exciton line (X) as well as two prominent biexciton resonances (XX1, XX2) are visible. The third biexciton (XX3) has a much smaller oscillator strength. d, Differential absorption from the fitting curves in c. Msymmetric lineshape, bleaching and shift of the exciton lead to the remarkable signature in $\Delta \alpha$ that is also observed in experiment. The shaded areas show the contributions of biexcitons and excitons to the differential signal.

Probe energy

1,710 1,720 1,730 1,740 1,750

Probe energy (meV)

of bound and scattering four-particle states. Biexciton binding energies $(E_{\rm B} = E_{\rm XX} - 2E_{\rm X})$ are then extracted by comparing the lowest eigenvalues of the full four-body problem (E_{xx}) to the exciton–exciton continuum edge $(2E_x)$ from a calculation for two independent excitons. Neglecting electron-hole exchange, the calculation yields a binding energy of 19.5 meV for the biexciton that is shown in Fig. 1a in freestanding monolayer WSe₂. We compare this result to previous variational calculations in the Supplementary Information, where we also show binding energies including electron-hole exchange for a freestanding monolayer. We find a correction of the largest biexciton binding energy proportional to the singlet-triplet exciton splitting Δ_{LP} as discussed before for materials such as CuCl and CdS11. In the presence of a dielectric environment of the TMDC monolayer given in experiment, where it is placed on a sapphire substrate, we obtain the biexciton binding energies {19.8, 12.3, 11.6, 11.6, 3.4, 3.1 meV. The arrangement of eigenenergies with three almost degenerate states in the middle is in good agreement with our configuration model as illustrated in Fig. 2d. Considering the optical selection rules discussed above, our microscopic theory thus predicts biexciton binding energies around 20, 12 and 3 meV to be NMTURE PHYSICS MRTICLES

observed in experiment. These values are in very good agreement with the binding energies we obtained from fitting the differential absorption spectra as shown in Fig. 3. The binding energies are only slightly overestimated by theory, most probably because screening by residual carriers is not taken into account.

Exchange interaction between electrons caused by their indistinguishability is at the heart of quantum mechanics and chemical bonding. Electrons and holes in a semiconductor, on the other hand, are approximately distinguishable, which generally results in weak electron-hole exchange effects. For example, in semiconductor quantum dots, the exciton fine structure due to electron-hole exchange is on the order of microelectronvolts, while in quantum wells no such effects have been observed. Our results show that atomically thin TMDC semiconductors are well suited to study the fine structure of correlated Coulomb complexes experimentally as these materials combine large binding energies and relatively strong electron-hole exchange interaction. Biexcitons reveal a distinct fine structure that can be traced back to electron-hole exchange, along with local-field corrections to biexciton binding energies. The fitting of experimental differential absorption spectra assuming three biexciton resonances, where the binding energies are very consistent at eight different pump wavelengths, strongly supports the predictions of our microscopic theory quantitatively. This is further supported by the fact that we can, at the same time, reproduce the complex differential line shape of the exciton resonance caused by biexciton correlations, which has not been reported before for TMDCs.

We further demonstrate that profound insight into the relevant interaction processes can be gained by condensing the full microscopic theory into a simple configuration model for biexcitons. From the observation that the simple model captures the structure of the full spectrum, we conclude that the latter is essentially determined by the spin-selection rules of electron-hole exchange, while precise numbers can be obtained from microscopic calculations. Our picture of many-body complexes and their fine structure goes beyond the frequently used classification of many-body states as a combination of bright and dark excitons from different valleys. The picture of a biexciton as a combination of two specific excitons corresponds to a single four-particle configuration in our scheme. The true many-body states observed in optical spectra emerge from the interaction of such configurations driven by electron-hole exchange.

The understanding of the biexciton fine structure opens a new field of research as the conclusions we draw are not limited to ${\rm WSe_2}$ on sapphire substrate but are general for most vertical heterostructures based on semiconducting TMDCs. Even richer fine structures are expected for molybdenum-based materials due to the practically degenerate conduction bands, where more biexciton configurations can take part in the interaction. The configuration picture we present here can moreover be extended to consider electron—hole exchange in dark—bright biexcitons and higher Coulomb complexes in TMDCs. The emergence of encapsulated samples with reduced linewidths, narrower than the splittings we predict here, promises to reveal this rich spectral structure in future experiments 40 .

The biexciton fine structure does not rely on the existence of several inequivalent valleys as a single spin-degenerate conduction- and valence-band valley should have the same effect. Such a situation is given for thallium halides, where a configuration picture has already been applied to determine the effect of electron-hole exchange on the lowest biexciton state¹². However, a biexciton fine structure has not been predicted there. Neither has it been attempted to calculate material-realistic spectra for classical materials with strong biexciton signatures such as CuCl. We conclude that reconsidering such materials by means of both modern computational and experimental methods could reveal previously undiscovered biexciton properties.

In light of our results, the question arises whether electron-hole exchange effects are carried over to TMDC nanostructures⁴¹⁻⁴³ or localized biexciton complexes⁴⁴ both envisaged for quantum-optical

applications. The biexciton fine structure in TMDC layers, as we describe it here, crucially depends on the existence of several four-particle configurations, due to the continuous density of states provided by the band-structure valleys, interacting via electron-hole exchange. If only a discrete density of states is realized in a nano-structure, we expect just a single biexciton line as in semiconductor quantum dots. However, the microscopic understanding of TMDC nanostructures and their electronic states is still at its very beginning and remains a fascinating topic for future investigations.

Online content

Any methods, additional references, Nature Research reporting summaries, source data, statements of data availability and associated accession codes are available at https://doi.org/10.1038/s41567-018-0282-x.

Received: 12 January 2018; Accepted: 20 August 2018; Published online: 1 October 2018

References

- Onodera, Y. & Toyozawa, Y. Excitons in alkali halides. J. Phys. Soc. Jpn 22, 833–844 (1967).
- Denisov, M. M. & Makarov, V. P. Longitudinal and transverse excitons in semiconductors. *Phys. Status Solidi B* 56, 9–59 (1973).
- Warming, T. et al. Hole-hole and electron-hole exchange interactions in single InAs/GaAs quantum dots. Phys. Rev. B 79, 125316 (2009).
- Kadantsev, E. & Hawrylak, P. Theory of exciton fine structure in semiconductor quantum dots: Quantum dot anisotropy and lateral electric field. *Phys. Rev. B* 81, 045311 (2010).
- Sieh, C. et al. Coulomb memory signatures in the excitonic optical Stark effect. Phys. Rev. Lett. 82, 3112–3115 (1999).
- Schäfer, W. & Wegener, M. Semiconductor Optics and Transport Phenomena (Springer, Berlin, New York, 2002).
- Forney, J. J., Quattropani, A. & Bassani, F. Electron-hole exchange contributions to the biexciton states. Il Nuovo Cimento B 22, 153–178 (1974).
- Quattropani, A., Forney, J. J. & Bassani, F. Biexcitons in indirect-gap semiconductors: applications to GaSe and AgBr. *Phys. Status Solidi B* 70, 497–504 (1975).
- Ekardt, W. & Sheboul, M. I. The influence of the electron-hole exchange interaction on the biexciton ground state in CuCl and CuBr. and related optical transitions. *Physica Status Solidi B* 73, 475–482 (1976).
- Bassani, F. & Rovere, M. Biexciton binding energy in Cu₂O. Solid State. Commun. 19, 887–890 (1976).
- Quattropani, A. & Forney, J. J. Theory. of excitonic molecules. Il Nuovo. Cimento. B. 39, 569–578 (1977).
- Chung, S. G., Sanders, G. D. & Chang, Y.-C. Theory of excitonic molecules in thallous halide: The role of electron-hole exchange interaction. *Solid State. Commun.* 45, 237–241. (1983).
- Ungier, W. Electron-hole exchange interaction in a biexciton molecule. Solid State Commun. 69, 53-55 (1989).
- 14. Yu, T. & Wu, M. W. Valley depolarization due to intervalley and intravalley electron-hole exchange interactions in monolayer MoS₂. Phys. Rev. B 89, 205303 (2014).
- Yu, H., Liu, G.-B., Gong, P., Xu, X. & Yao, W. Dirac cones and Dirac saddle points of bright excitons in monolayer transition metal dichalcogenides. *Nat. Commun.* 5, 3876 (2014).
- Glazov, M. M. et al. Spin and valley dynamics of excitons in transition metal dichalcogenide monolayers. *Phys. Status Solidi B* 252, 2349–2362 (2015).
- Schmidt, R. et al. Ultrafast Coulomb-induced intervalley coupling in atomically thin WS₂. Nano. Lett. 16, 2945–2950 (2016).
- Hao, K. et al. Direct measurement of exciton valley coherence in monolayer. WSe₂. Nat. Phys. 12, 677–682 (2016).
- Qiu, D. Y., Cao, T. & Louie, S. G. Nonanalyticity, valley quantum phases, and lightlike exciton dispersion in monolayer transition metal dichalcogenides: theory and first-principles calculations. *Phys. Rev. Lett.* 115, 176801 (2015).
- Jones, A. M. et al. Excitonic luminescence upconversion in a two-dimensional semiconductor. Nat. Phys. 12, 323–327 (2016).
- Plechinger, G. et al. Trion fine structure and coupled spin-valley dynamics in monolayer tungsten disulfide. *Nat. Commun.* 7, 12715–12723 (2016).
- Singh, A. et al. Long-lived valley polarization of intravalley trions in monolayer. WSe₂. Phys. Rev. Lett. 117, 257402 (2016).
- Voss, T., Rückmann, I., Gutowski, J., Axt, V. M. & Kuhn, T. Coherent control
 of the exciton and exciton-biexciton transitions in the generation of
 nonlinear wave-mixing signals in a semiconductor quantum well. *Phys. Rev. B*73, 115311 (2006).

- Gilliot, P. et al. Measurement of exciton spin coherence by nondegenerate four-wave mixing experiments in the χ⁽³⁾ regime. *Phys. Rev. B* 75, 125209 (2007).
- Mayers, M. Z., Berkelbach, T. C., Hybertsen, M. S. & Reichman, D. R. Binding energies and spatial structures of small carrier complexes in monolayer transition-metal dichalcogenides via diffusion Monte Carlo. *Phys. Rev. B* 92, 161404 (2015).
- Zhang, D. K., Kidd, D. W. & Varga, K. Excited biexcitons in transition metal dichalcogenides. Nano Lett. 15, 7002–7005 (2015).
- Kylänpää, I. & Komsa, H.-P. Binding energies of exciton complexes in transition metal dichalcogenide monolayers and effect of dielectric environment. *Phys. Rev. B* 92, 205418 (2015).
- Szyniszewski, M., Mostaani, E., Drummond, N. D. & Fal'ko, V. I. Binding energies of trions and biexcitons in two-dimensional semiconductors from diffusion quantum Monte Carlo calculations. *Phys. Rev. B* 95, 081301 (2017).
- Hao, K. et al. Neutral and charged inter-valley biexcitons in monolayer MoSe₂. Nat. Commun. 8, 15552 (2017).
- Mai, C. et al. Many-body effects in valleytronics: direct measurement of valley lifetimes in single-layer MoS₂. Nano. Lett. 14, 202–206 (2014).
- You, Y. et al. Observation of biexcitons in monolayer WSe2. Nature Physics 11, 477–481. (2015).
- Plechinger, G. et al. Identification of excitons, trions and biexcitons in single-layer. WS₂. Phys. Status Solidi Rapid Res. Lett. 9, 457–461 (2015).
- Shang, J. et al. Observation of excitonic fine structure in a 2D transitionmetal dichalcogenide semiconductor. ACS Nano 9, 647–655 (2015).
- Sie, E. J., Frenzel, A. J., Lee, Y.-H., Kong, J. & Gedik, N. Intervalley. biexcitons and many-body effects in monolayer. MoS₂. Phys. Rev. B 92, 125417 (2015).
- Lee, H. S., Kim, M. S., Kim, H. & Lee, Y. H. Identifying multiexcitons in MoS₂ monolayers at room temperature. *Phys. Rev. B* 93, 140409 (2016).
- Okada, M. et al. Observation of biexcitonic emission at extremely low power density in tungsten disulfide atomic layers grown on hexagonal boron nitride. Sci. Rep. 7, 322 (2017).
- Van Tuan, D., Scharf, B., Žutić, I. & Dery, H. Marrying excitons and plasmons in monolayer transition-metal dichalcogenides. *Phys. Rev. X* 7, 041040 (2017).
- Xu, X., Yao, W., Xiao, D. & Heinz, T. F. Spin and pseudospins in layered transition metal dichalcogenides. Nat. Phys., 10, 343–350 (2014).
- Hulin, D. & Joffre, M. Excitonic optical stark redshift: the biexciton signature. Phys. Rev. Lett. 65, 3425–3428 (1990).
- Tran, K. et al. Disorder-dependent valley properties in monolayer. WSe₂. Phys. Rev. B 96, 041302 (2017).

- Kern, J. et al. Nanoscale positioning of single-photon emitters in atomically. thin WSe₂. Adv. Mater. 28, 7101–7105 (2016).
- Branny, A., Kumar, S., Proux, R. & Gerardot, B. D. Deterministic straininduced arrays of quantum emitters in a two-dimensional semiconductor. *Nat. Commun.* 8, 15053 (2017).
- Palacios-Berraquero, C. et al. Large-scale quantum-emitter arrays in atomically thin semiconductors. Nat. Commun. 8, 15093 (2017).
- He, Y.-M. et al. Cascaded emission of single photons from the biexciton in monolayered WSe₂. Nat. Commun. 7, 13409 (2016).

⋈ cknowledgements

This work was supported by Deutsche Forschungsgemeinschaft (DFG) within CRC 1558 and RTG 2247. A.W.A. acknowledges funding from DFG via grant no. AC290-2/1. The spectroscopic experiments were jointly supported by NSF DMR1306878 (A. Singh) and the NSF MRSEC program DMR-1720595 (K.T.). X.L. gratefully acknowledges support from the Welch foundation (F-1662) and the Alexander von Humboldt Foundation, which facilitated the collaboration with TU-Berlin. A. Steinhoff and M.F. would like to acknowledge P. Gartner for fruitful discussions. We thank G. Schönhoff, M. Rösner and T. Wehling for providing material-realistic band structures and bare as well as screened Coulomb matrix elements.

Muthor contributions

A. Steinhoff and M.F. performed analytical and numerical calculations of the biexciton spectra. A. Singh, K.T. and M.K. designed and performed the experiments... K.T. exfoliated the sample. N.O., A. Singh, A.W.A. and S.H. analysed the data. N.O., A. Steinhoff, M.F. and A. Singh prepared the manuscript. U.W., F.J. and X.L. initiated and coordinated the project. All authors contributed to the discussion and the writing of the manuscript.

Competing interests

The authors declare no competing interests.

M dditional information

Supplementary information is available for this paper at https://doi.org/10.1038/s41567-018-0282-x.

Reprints and permissions information is available at www.nature.com/reprints.

Correspondence and requests for materials should be addressed to A.S.

Publisher's note: Springer. Nature remains neutral with regard to jurisdictional claims in published maps and institutional affiliations.

NM TURE PHYSICS MRTICLES

Methods

Dynamics-controlled truncation theory for biexcitons including electron–hole exchange. The equations that describe coherent biexcitons in a pump–probe setup on a microscopic basis are derived using the dynamics-controlled truncation scheme^{45,46} that has been successfully used in the past to describe biexcitonic effects in quantum-well structures⁵. This method allows one to systematically account for nonlinear contributions to exciton dynamics up to a certain order in the exciting optical fields within the coherent limit. Biexcitonic contributions appear in third order (χ ⁵) nonlinearity) and the biexciton spectrum is governed by the homogeneous equations of motion for the four-particle correlations

$$B_{\mathbf{k},\mathbf{k}'}^{hch'\epsilon'}(\mathbf{q}) := \langle a_{-\mathbf{k}'-\mathbf{q}}^{h'} a_{\mathbf{k}'}^{\epsilon'} a_{-\mathbf{k}}^{h} a_{\mathbf{k}+\mathbf{q}}^{\epsilon} \rangle$$

$$-\langle a_{-\mathbf{k}'-\mathbf{q}}^{h'} a_{\mathbf{k}'}^{\epsilon} \rangle \langle a_{-\mathbf{k}}^{h} a_{\mathbf{k}+\mathbf{q}}^{\epsilon} \rangle$$
(4)

with electron and hole annihilation operators $a_{\mathbf{k}}^{e}$ and $a_{\mathbf{k}}^{h}$.

$$i\hbar \frac{d}{dt} B_{k,k}^{heh'e'}(\mathbf{q}) = (\varepsilon_{-\mathbf{k}-\mathbf{q}}^{h'} + \varepsilon_{\mathbf{k}}^{e'} + \varepsilon_{-\mathbf{k}}^{h} + \varepsilon_{\mathbf{k}+\mathbf{q}}^{e}) B_{k,k}^{heh'e'}(\mathbf{q})$$

$$- \frac{1}{\mathcal{A}} \sum_{\mathbf{q}'h'e'} (V_{k,k+\mathbf{q}-\mathbf{q}',k'+\mathbf{q},k'-\mathbf{q}'}^{e'h'h'e'} + V_{k,k+\mathbf{q}-\mathbf{q}',k'+\mathbf{q}',k'+\mathbf{q}}^{e'h}) B_{k,k'-\mathbf{q}'}^{heh'e'}(\mathbf{q})$$

$$- U_{k,k'+\mathbf{q}-\mathbf{q}',k'-\mathbf{q}',k'+\mathbf{q}}^{e'heh} B_{k,k'-\mathbf{q}'}^{heh'e'}(\mathbf{q})$$

$$- \frac{1}{\mathcal{A}} \sum_{\mathbf{q}'he'} (V_{k+\mathbf{q},k-\mathbf{q}',k}^{e'heh} B_{k-\mathbf{q}',k'}^{e'heh'e'}(\mathbf{q})$$

$$+ \frac{1}{\mathcal{A}} \sum_{\mathbf{q}'h'e'} V_{k+\mathbf{q}+\mathbf{q}',k-\mathbf{q}',k,k'-\mathbf{q}'}^{h'hhh'} B_{k-\mathbf{q}',k'}^{heh'e'}(\mathbf{q}+\mathbf{q}')$$

$$- \frac{1}{\mathcal{A}} \sum_{\mathbf{q}'h'e'} (V_{k,k-\mathbf{q}',k,k'-\mathbf{q}'}^{e'hhe'} - U_{k,k-\mathbf{q}',k'-\mathbf{q}',k'}^{e'he'})$$

$$+ \frac{1}{\mathcal{A}} \sum_{\mathbf{q}'h'e'} (V_{k+\mathbf{q},k'+\mathbf{q}-\mathbf{q}',k'+\mathbf{q}-\mathbf{q}',k'+\mathbf{q}-\mathbf{q}',k'+\mathbf{q}-\mathbf{q}'}^{e'he'h'e'}(\mathbf{q}-\mathbf{q}')$$

$$- \frac{1}{\mathcal{A}} \sum_{\mathbf{q}'h'e'} (V_{k+\mathbf{q},k'+\mathbf{q}-\mathbf{q}',k'+\mathbf{q}-\mathbf{q}',k'+\mathbf{q}-\mathbf{q}',k'+\mathbf{q}-\mathbf{q}'}^{e'h'e'})$$

$$- \frac{1}{\mathcal{A}} \sum_{\mathbf{q}'h'e'} (V_{k+\mathbf{q},k'+\mathbf{q}-\mathbf{q}',k'+\mathbf{q}-\mathbf{q}',k'+\mathbf{q}-\mathbf{q}',k'+\mathbf{q}-\mathbf{q}'}^{e'h'e'})$$

$$- U_{k+\mathbf{q},k'+\mathbf{q}-\mathbf{q}',k'+\mathbf{q}-\mathbf{q}',k'+\mathbf{q}-\mathbf{q}',k'+\mathbf{q}-\mathbf{q}'}^{e'h'e'}$$

$$- U_{k+\mathbf{q},k'+\mathbf{q}-\mathbf{q}',k'+\mathbf{q}-\mathbf{q}',k'+\mathbf{q}-\mathbf{q}',k'+\mathbf{q}-\mathbf{q}'}^{e'h'e'}$$

$$- U_{k+\mathbf{q},k'+\mathbf{q}-\mathbf{q}',k'+\mathbf{q}-\mathbf{q}',k'+\mathbf{q}-\mathbf{q}',k'+\mathbf{q}-\mathbf{q}'}^{e'h'e'}$$

A denotes the crystal area. Equation (5) represents a generalized four-particle Schrödinger equation for zero total momentum in reciprocal space including arbitrary band structures ε_k^{λ} and Coulomb matrix elements $V_{k+q,k'-q,k',k}^{\lambda_1\lambda_2\lambda_2\lambda_2}$. While the band structures are given in the electron–hole picture with hole momenta written as negative valence electron momenta, the matrix elements are represented in the picture of conduction and valence band electrons as usually obtained from first-principle. calculations. The six 'direct' interaction terms with matrix elements V and momentum transfer.q' are analogous to Coulomb interaction between the four particles in a hydrogen molecule. The additional terms describe electron-hole exchange, which is beyond the picture of biexcitons as a semiconductor counterpart to hydrogen. molecules. As the Coulomb interaction is spin-diagonal, only the electron-hole exchange terms couple biexcitons with different spin combinations. We consider the two highest conduction and two lowest valence bands of a TMDC semiconductor here, hence e and h label the respective spin index. Otherwise there would be additional exchange terms between different conduction and different valence bands in equation (5). Note that the electron-hole exchange interaction is described by unscreened. Coulomb matrix elements U (see refs 2,19,47), while V denotes matrix elements screened. by carriers in occupied bands and the dielectric environment of the TMDC layer. The first three lines of equation (5) describe two independent excitons containing the exciton-exciton continuum edge as the lowest eigenstate.

As those TMDC biexcitons visible in pump-probe experiments are hosted in the K and K' valleys of the Brillouin zone, we limit our single-particle basis to these valleys, where we carefully converge our results with respect to the radius in k-space around K and K' and to the resolution of the used Monkhorst-Pack mesh. More details on the convergence are given in the Supplementary Information. To obtain biexciton spectra numerically, we have to diagonalize the homogeneous equation of motion (5) in a matrix form set up in a basis defined by the quantum numbers $\{k, k', q, e, h, e', h'\}$. Since the resulting matrix can amount up to several terabytes depending on the used k-mesh, we utilize an iterative Krylov space method as contained in the SLEPc package⁶⁶ for the PETSc toolkit⁶⁹ to obtain only the lowest eigenvalues. Due to the numerical discretization of momentum space, there is an uncertainty of binding energies of ± 1 .meV.

Material-realistic description of Coulomb interaction. We combine the above many-body theory of biexcitons with ab initio methods providing materialrealistic band structures and bare as well as screened Coulomb matrix elements on a GoWo level as input for the equations of motion (5). More details on the G₀W₀ calculations are given in ref. 50. The valence- and conduction-band splitting caused by spin-orbit interaction is described along the lines of refs 50,51 including first- and second-order effects. Coulomb matrix elements for monolayer WSe, on a substrate are obtained in two steps. First, density functional theory ground-state data for a freestanding monolaver obtained in FLEUR⁵² are used to calculate bare Coulomb matrix elements and the RPA dielectric function in the SPEX⁵³ code. The quantities are calculated in a localized basis $|\alpha\rangle$ consisting of Wannier functions with dominant W-d-orbital character for discrete values of momentum q. Then, bare matrix elements and the dielectric function including substrate effects are parametrized as a function of |q| using the Wannier function continuum electrostatics approach described in refs 54,55... The approach combines a continuum electrostatic model for the screening by the dielectric environment in a heterostructure with a localized description of Coulomb interaction. The actual parametrization is provided in ref. 56. To simulate the dielectric environment given in our experiment, we assume that the WSe2 layer is van der Waals-bound to the sapphire substrate with dielectric constant $\varepsilon = 10$ and a distance of 3.Å between the outer atomic layers of the TMDC and the substrate, which has been shown to be reasonable 55,57. We obtain Coulomb matrix elements in Bloch-state representation by a unitary transformation

$$U_{\mathbf{k}+\mathbf{q},\mathbf{k}'-\mathbf{q},\mathbf{k}',\mathbf{k}}^{\lambda_{1}\lambda_{2}\lambda_{3}\lambda_{4}} = \sum_{\alpha\beta\gamma\delta} \left(c_{\alpha,\mathbf{k}+\mathbf{q}}^{\lambda_{1}}\right)^{*} \left(c_{\beta,\mathbf{k}'-\mathbf{q}}^{\lambda_{2}}\right)^{*} c_{\gamma,\mathbf{k}}^{\lambda_{3}} c_{\delta,\mathbf{k}}^{\lambda_{4}} U_{\mathbf{q}}^{\alpha\beta\gamma\delta}$$

$$\tag{6}$$

with coefficients $c_{a,k}^{\lambda}$ that connect the localized and the Bloch basis on a G_0W_0 level as described previously 50 . While for the direct Coulomb interaction density–density–like contributions $V_{\bf q}^{a\beta\beta\alpha}$ are dominant, it turns out that a proper description of electron–hole exchange additionally requires matrix elements that are exchange–like in the local representation:

$$U_{\mathbf{q}}^{a\beta\gamma\delta} = U_{\mathbf{q}}^{a\beta\beta\alpha} \delta_{\alpha\delta} \delta_{\beta\gamma} + U^{\alpha\beta\alpha\beta} \delta_{\alpha\gamma} \delta_{\beta\delta}$$
 (7)

The density-density-like matrix elements given in the first term are momentum-dependent and thus nonlocal in real space with a characteristic 1/q behaviour for small momenta. A numerical analysis shows that they yield the main contribution to the longitudinal-transverse exciton splitting shown in Supplementary Fig. 2 that leads to a light-like dispersion of the upper exciton branch. The exchange-like matrix elements in the second term of equation (7), on the other hand, are practically momentum-independent and correspond to local interaction processes between carriers within the same unit cell. They alone are responsible for the almost momentum-independent exciton blueshift, which is therefore termed a local-field effect. Unlike the density-density-like matrix elements, the exchange-like matrix elements are not obtained via the Wannier function continuum electrostatics approach but fitted directly with a constant value.

The exchange effects can also be understood by analysing Coulomb matrix elements such as $U_{\mathbf{k}+\mathbf{q},\mathbf{k}-\mathbf{q}',\mathbf{k}+\mathbf{q}-\mathbf{q}',\mathbf{k}}^{h\,eh}$ in equation (5) for \mathbf{k} and $\mathbf{k}-\mathbf{q}'$ in the vicinity. of K and K' and small exciton momenta q. To this end, we resort to the $d_{\mathrm{m=0}}$ and $d_{m=+2}$ orbital character of Bloch states in the K- and K'-valleys as obtained analytically from a simple lattice model^{38,58}. It turns out that index combinations. $U^{\alpha\beta\beta\alpha}$ lead to intra- and inter-valley exchange terms that scale linearly with |q|, while combinations $U^{a\beta a\beta}$ yield intra-valley terms that have constant and quadratic contributions. A similar discussion of electron-hole exchange in much detail has been led by Qiu et al. 19 for monolayer MoS2, with the difference that they use a plane-wave description of Coulomb interaction. In monolayer WSe2, the exchange-like matrix elements, if normalized to a unit-cell area, amount to 0.39 eV. for interaction between $d_{m=0}$ and $d_{m=+2}$ orbitals and to 0.19.eV for interaction. among $d_{m=\pm 2}$ orbitals. These matrix elements are obtained from combined density. functional theory and GW calculations as described above, where the momentumdependence is found to be negligible. Moreover, we find that matrix elements involving three different orbitals that would in principle additionally contribute to the above-mentioned effects are negligible with respect to the other ones.

Simplified model of electron–hole exchange. Equation (5) constitutes a four-particle Hamiltonian whose eigenstates describe biexcitons with vanishing total momentum. The Hamiltonian can be split into a part without electron–hole exchange $H_{\rm D}$, a part including nonlocal exchange $H_{\rm D}$ and a local-field part $H_{\rm LP}$ according to the Coulomb matrix elements V, U^{appa} and U^{apaq} involved, see equation (7). The four-particle configurations

 $\{|B_{KK}^{\uparrow\uparrow\uparrow\uparrow}(0)\rangle, |B_{KK}^{\uparrow\uparrow\uparrow\downarrow}(0)\rangle, |B_{KK}^{\downarrow\uparrow\uparrow\uparrow}(0)\rangle, |B_{KK}^{\downarrow\uparrow\downarrow\uparrow}(-K)\rangle, |B_{KK}^{\downarrow\uparrow\uparrow\downarrow}(K)\rangle, |B_{KK}^{\downarrow\uparrow\downarrow\uparrow}(0)\rangle\}$ are eigenstates of H_0 with eigenenergies E. These configurations with carrier spins as upper indices are superpositions of four-particle states $B^{he\uparrow}(q)$ given by the quasi-momenta -k, k+q, k' and -k'-q as evident from equation (5). The configurations can also be seen as superpositions of two-exciton states with different exciton momenta. This is expressed by the lower configuration indices denoting the valleys where the excitons reside, while the dominant exciton

momentum q is given in brackets. Electron—hole exchange introduces off-diagonal matrix elements $\langle B_i | H_U + H_{LF} | B_j \rangle = U_{ij} + \Delta_{LF,ij}$. Taking into account the electron and hole spins in the basis configurations, we can determine those exchange matrix elements that do not flip carrier spins and are thus non-zero. The matrix elements U_{ij} and $\Delta_{LE,ij}$ are projections of the microscopic four-particle Hamiltonian into the configuration basis and therefore incorporate electron—hole exchange between carriers with all possible momenta according to their admixture in the respective biexciton state. Therefore, they are in principle based on the material-realistic Coulomb matrix elements obtained from first principles. Since we use the configuration model only for a qualitative discussion, we do not attempt to obtain explicit values for U_{ij} and $\Delta_{LE,ij}$. As a simplification, we assume that all non-zero exchange matrix elements have the same values U and Δ_{LF} respectively. Then the full Hamiltonian in the subspace of bound biexcitons is given as a 6×6 matrix by

Biexciton energies E without electron–hole exchange appear as diagonal entries together with twice the exchange matrix element U, as each biexciton state allows for at least two different exchange processes between like-spin electron–hole pairs. The second matrix takes care of all possible interaction processes between the biexciton configurations and the final one accounts for the local-field shifts of those states that contain two like-spin excitons (see Fig. 2a), which excludes configurations 4 and 5. To obtain a clear picture, we diagonalize the matrix H_1 without local-field contributions, which we include afterwards using perturbation theory. The eigenenergies of H_1 are given by $E_i = \{E, E+2U, E+2U, E+2U, E+4U, E+6U\}$ and the corresponding eigenstates $|\Phi_i\rangle$ are $1/\sqrt{6}(1,-1,-1,-1,-1,1)^T$, $1/2(0,1,1,-1,-1,0)^T$, $1/\sqrt{2}(1,0,0,0,0,-1)^T$. and $1/\sqrt{12}(2,1,1,1,1,2)^T$. The first-order energy correction to the lowest eigenenergy is $\langle \Phi_i | H_{I_1F} | \Phi_i \rangle = 4/3\Delta_{I_1F}$.

Sample characterization. On the basis of previous studies of similarly prepared samples⁵⁹, we consider that the sample is n-doped. The electronic structure of the sample is characterized by exciting photoluminescence with a helium neon laser (632.8.nm), and measuring the differential absorption, using the output of a titanium–sapphire laser tuned across the A exciton and trion resonances of the sample. In both cases, we obtain spectra with clearly pronounced inhomogeneously broadened signatures of the neutral exciton and the two overlapping trions. More details are given in the Supplementary Information.

Pump-probe experiment. The experiments are carried out by splitting the output of a titanium-sapphire laser into a pump and a probe beam. The output pulses have a spectral full-width at half-maximum (FWHM) of 15 nm. Their spectra are shaped in two grating-based pulse-shapers using an amplitude mask to a spectral width of about 0.7 nm FWHM, corresponding to a duration of about 1 ps FWHM. in time. The intensity of both beams is modulated by passing them through acousto-optical modulators driven at about 3.MHz with a difference of a few. kilohertz.. Polarization control is carried out by linear polarizers and subsequent quarter-wave plates. The beams are overlapped spatially in a beamsplitter cube and focused on the sample by a 50x microscope objective with a numerical aperture of 0.42 to a spot size of 2 µm in diameter. Intensity-dependent studies are performed to ensure that the data taken at $\approx 10 \,\mu\text{W}$ are in the $\chi^{(3)}$ regime and to avoid excessive heating. After passing through the sample, the pump part is filtered out by a monochromator. The differential transmission is detected by a silicon detector. coupled to a lock-in amplifier set to the difference frequency of the pump and probe modulations. Assuming no purely reflection-related resonances, this can be directly correlated to the negative differential absorption.

Bandgap renormalization effects. From the fitting of experimental spectra, in most cases we extract a small exciton redshift below 1.meV, which points to dominant biexcitonic effects on the line shift. Line shifts caused by bandgap renormalization effects, which are due to exchange interaction, are largely suppressed in cross-polarized pump-probe spectra as the pump and probe pulses

address electronic states with opposite spin. In TMDC semiconductors, inter-valley, scattering of excitons due to electron-hole exchange may induce bandgap, renormalizations in cross-polarized pump-probe on the picosecond timescale¹⁷. This effect is ruled out by taking differential absorption spectra at zero time delay. Independent of their magnitude, none of the discussed renormalizations would induce a splitting of lines, but influence only energetic positions and linewidths.

Signatures of dark excitons. The conduction-band spin-orbit splitting in monolayer WSe₂ facilitates the formation of dark K-valley excitons as well as corresponding biexcitons. Spectrally, the dark excitons are located below the trions⁶¹⁻⁶³, while dark biexcitons are expected to be found at even lower energies. On the other hand, dark-bright biexcitons composed of one dark and one bright exciton are expected to be spectrally located between excitons and trions. For the creation of these complexes, however, the relaxation of one bright exciton created by the pump pulse into a dark state is necessary, which requires either a spin flip or inter-valley scattering. The lower limit for the timescale of both processes is set by the observed decay of exciton polarization, in our case about 1.9 ps (see the discussion in the Supplementary, Information). Hence, at zero pump-probe delay time, the contribution of these processes can be expected to be minor compared to the coherently created bright-bright complexes.

Data availability

The data that support the plots within this paper and other findings of this study are available from the corresponding author upon reasonable request.

References

- Axt, V. M. & Stahl, A. A dynamics-controlled truncation scheme for the hierarchy of density matrices in semiconductor optics. Z. Phys. B 93, 195–204 (1994).
- Lindberg, M., Hu, Y. Z., Binder, R. & Koch, S. W. X⁽³⁾ formalism in optically excited semiconductors and its applications in four-wave-mixing spectroscopy. *Phys. Rev. B*. 50, 18060. (1994).
- Sham, L. J. & Rice, T. M. Many-particle derivation of the effective-mass equation for the Wannier exciton. *Phys. Rev.* 144, 708–714 (1966).
- Hernandez, V., Roman, J. E. & Vidal, V. SLEPc: a scalable and flexible toolkit for the solution of eigenvalue problems. ACM. Trans. Math. Softw. 31, 351–362 (2005).
- Balay, S. et al. Portable, extensible toolkit for scientific computation. Argonne National Laboratory. http://www.mcs.anl.gov/petsc/. (2018).
- Steinhoff, A., Rösner, M., Jahnke, F., Wehling, T. O. & Gies, C. Influence of excited carriers on the optical and electronic properties of MoS₂. Nano Lett.. 14, 3743–3748 (2014).
- Liu, G.-B., Shan, W.-Y., Yao, Y., Yao, W. & Xiao, D. Three-band tight-binding model for monolayers of group-VIB transition metal dichalcogenides. *Phys. Rev. B* 88, 085433 (2013).
- FLEUR: The Jülich FLAPW code family. FLEUR http://www.flapw.de/pm/index.php (2018).
- Friedrich, C., Blügel, S. & Schindlmayr, A. Efficient implementation of the GW. approximation. within the all-electron FLAPW method. *Phys. Rev. B*. 81, 125102 (2010).
- Rösner, M., Şaşıoğlu, E., Friedrich, C., Blügel, S. & Wehling, T. O. Wannier. function approach to realistic Coulomb interactions in layered materials and heterostructures. *Phys. Rev. B* 92, 085102 (2015).
- Florian, M. et al. The dielectric impact of layer distances on exciton and trion binding energies in van der Waals heterostructures. *Nano Lett.* 18, 2725–2732 (2018).
- Steinhoff, A. et al. Exciton fission in monolayer transition metal. dichalcogenide semiconductors. Nat. Commun. 8, 1166 (2017).
- Rooney, A. P. et al. Observing imperfection in atomic interfaces for van der. Waals heterostructures. Nano Lett. 17, 5222–5228 (2017).
- Xiao, D., Yao, W. & Niu, Q. Valley-contrasting physics in graphene: magnetic moment and topological transport. *Phys. Rev. Lett.* 99, 236809 (2007).
- Singh, A. et al. Trion formation dynamics in monolayer transition metal dichalcogenides. *Phys. Rev. B* 93, 041401 (2016).
- Combescot, M. & Combescot, R. Excitonic Stark shift: a coupling to semivirtual biexcitons. *Phys. Rev. Lett.* 61, 117–120 (1988).
- Wang, G. et al. In-plane propagation of light in transition metal dichalcogenide monolayers: optical selection rules. *Phys. Rev. Lett.* 119, 047401 (2017).
- Zhang, X.-X. et al. Magnetic brightening and control of dark excitons in monolayer WSe₂. Nat. Nanotech. 12, 883–888 (2017).
- Danovich, M., Zólyomi, V. & Fal'ko, V. I. Dark trions and biexcitons in WS₂ and WSe₂ made bright by e-e scattering. Sci. Rep. 7, 45998 (2017).